PHYSICAL REVIEW D **95,** 054503 (2017)

Locations of Roberge-Weiss transition endpoints in lattice QCD with $N_f = 2$ improved Kogut-Susskind quarks

Liang-Kai Wu*

Faculty of Science, Jiangsu University, Zhenjiang 212013, People's Republic of China

Xiang-Fei Meng

National Supercomputer Center in Tianjin, Tianjin 300457, People's Republic of China

(Received 11 December 2016; published 6 March 2017)

Result on locations of the tricritical points of $N_f = 2$ lattice QCD with imaginary chemical potential is presented. Simulations are carried out with Symanzik improved gauge action and Asqtad fermion action. With imaginary chemical potential $i\mu_I = i\pi T$, previous studies show that the Roberge-Weiss (RW) transition endpoints are triple points at both large and small quark masses, and second order transition points at intermediate quark masses. The triple and second order endpoints are separated by two tricritical ones. Our simulations are carried out at 7 values of quark mass am ranging from 0.024 to 0.070 on lattice volume $12^3 \times 4$, $16^3 \times 4$, $20^3 \times 4$. The susceptibility and Binder cumulant of the imaginary part of the Polyakov loop are employed to determine the nature of RW transition endpoints. The simulations suggest that the two tricritical points are within the range 0.024–0.026 and 0.040–0.050, respectively.

DOI: 10.1103/PhysRevD.95.054503

I. INTRODUCTION

The phase diagram of QCD has significantly phenomenological implications. It is relevant to the early Universe, compact stars, and heavy ion collision experiments. Reviews on the study of phase diagram can be found in Refs. [1,2] and references therein. While substantial lattice simulation has focused on the phase of QCD at finite density, a great amount of study centers around QCD with imaginary chemical potential. QCD with imaginary chemical potential has a rich phase structure, and it not only deserves detailed investigations in its own right theoretically, but also has significant relevance to physics at zero or small real chemical potential [3–11].

The Z(3) symmetry which is present in the pure gauge theory is explicitly broken at the presence of dynamical quarks. However, Ref. [12] shows that the Z(3) symmetry is restored when imaginary chemical potential is turned on and Z(3) transformation can be compensated by a shift in μ_I/T by $2\pi/3$, so the partition function of QCD with imaginary chemical potential has periodicity in μ_I/T with period $2\pi/N_c$ as well as reflection symmetry in $\mu = i\mu_I$.

Different Z(3) sectors are distinguished by the phase of the Polyakov loop. At high temperature, the spontaneous breaking of Z(3) symmetry implies transition between adjacent Z(3) sectors in μ_I and this transition is of first order, while at low temperature, unbroken Z(3) symmetry guarantees the transition is analytic. The first order transition takes place at those critical values of imaginary chemical potential $\mu_I/T = (2n+1)\pi/3$ [12–14]. At high temperature, those first order transition points form a transition line which necessarily ends at an endpoint T_{RW} when the temperature is decreased sufficiently low.

Recent numerical studies [3–5,15,16] show that the RW transition endpoints are triple points for small and heavy quark masses, and second order points for intermediate quark masses. So there exist two tricritical points separating the first order transition points from the second ones. Moreover, it is pointed out [3,10,11] that the scaling behavior at the tricritical points may shape the critical line which separates different transition region for real chemical potential, and thus, the critical line for real chemical potential is expected to be qualitatively consistent with the scenario suggested in Refs. [17,18] which shows that the first order transition region shrinks with increasing real chemical potential. In addition, Ref. [19] employs the scaling behavior at the tricritical point to determine the nature of 2 flavor QCD transition in the chiral limit.

So far, the investigation for the Roberge-Weiss (RW) transition endpoints is implemented through standard gauge and fermion actions. In this paper, we aim to investigate the endpoints of $N_f = 2$ QCD with one-loop Symanzik-improved gauge action [20–23] and Asqtad Kogut-Susskind action [24,25]. These actions have discretization errors of $O(\alpha_s^2 a^2, a^4)$ and $O(\alpha_s a^2, a^4)$, respectively. These improvements are significant on $N_t = 4$ lattice where the lattice spacing is quite large. Standard Kogut-Susskind fermions suffer from taste symmetry breaking at nonzero lattice spacing a [26]. This taste symmetry breaking can be illustrated by the smallest pion mass taste splitting which is comparable to the pion mass even at lattice spacing $a \sim 0.1$ fm [27]. Asqtad Kogut-Susskind action has good taste symmetry and free

*Corresponding author.
wuliangkai@163.com

dispersion relation by introducing fattened links and the so-called "Naik terms" [28,29].

The paper is organized as follows. In Sec. II, we define the lattice action with imaginary chemical potential and the physical observables we calculate. Our simulation results are presented in Sec. III followed by discussions in Sec. IV.

II. LATTICE FORMULATION WITH IMAGINARY CHEMICAL POTENTIAL

After introducing pseudofermion field Φ, the partition function of the system can be represented as:

$$Z = \int [dU][d\Phi^*][d\Phi] e^{-S_g - S_f},$$

where S_g is the Symanzik-improved gauge action, and S_f is the Asqtad quark action with the quark chemical potential μ. Here $\mu = i\mu_I$. For S_g, we use

$$S_G = \beta\Big(C_P \sum_{x;\mu<\nu}(1 - P_{\mu\nu}) + C_R \sum_{x;\mu\neq\nu}(1 - R_{\mu\nu}) + C_T \sum_{x;\mu<\nu<\sigma}(1 - T_{\mu\nu\sigma})\Big),$$

with $P_{\mu\nu}$, $R_{\mu\nu}$ and $T_{\mu\nu\sigma}$ standing for $1/3$ of the imaginary part of the trace of 1×1, 1×2 planar Wilson loops and $1\times1\times1$ "parallelogram" loops, respectively.

$P_{\mu\nu} = \frac{1}{3}\mathrm{ReTr}$  ,

$R_{\mu\nu} = \frac{1}{3}\mathrm{ReTr}$ 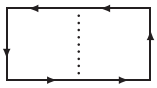 ,

$T_{\mu\nu\sigma} = \frac{1}{3}\mathrm{ReTr}$ 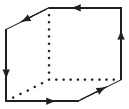 .

The coefficients C_P, C_R, C_T are tadpole improved [27],

$$C_P = 1.0,$$
$$C_R = \frac{-1}{20u_0^2}(1 - (0.6264 - 1.1746n_f)\ln(u_0)),$$
$$C_T = \frac{1}{u_0^2}(0.0433 - 0.0156n_f)\ln(u_0).$$

The Asqtad action with pseudofermion field Φ is

$$S_f = \langle\Phi|[M^\dagger[U]M[U]]^{-n_f/4}|\Phi\rangle,$$

where the form of $M_{x,y}[U] = 2m_{x,y} + D_{x,y}(U)$ reading

$$\begin{aligned} &2m\delta_{x,y} + \sum_{\rho=1}^{3}\eta_{x,\rho}(U^F_{x,\rho}\delta_{x,y-\hat\rho} - U^{F\dagger}_{x-\hat\rho,\rho}\delta_{x,y+\hat\rho}) \\ &+ \eta_{x,4}(e^{ia\mu_I}U^F_{x,4}\delta_{x,y-\hat4} - e^{-ia\mu_I}U^{F\dagger}_{x-\hat4,\mu}\delta_{x,y+\hat4}) \\ &+ \sum_{\rho=1}^{3}\eta_{x,\rho}(U^L_{x,\rho}\delta_{x,y-3\hat\rho} - U^{L\dagger}_{x-\rho,\rho}\delta_{x,y+3\hat\rho}) \\ &+ \eta_{x,4}(e^{i3a\mu_I}U^L_{x,4}\delta_{x,y-3\hat4} - e^{-i3a\mu_I}U^{L\dagger}_{x-\hat4,\mu}\delta_{x,y+3\hat4}), \end{aligned}$$

where $U^F_{x,\rho}$ stands for the fattened link which is produced by Fat7 smearing and $U^L_{x,\rho}$ stands for the naik term. $\hat\rho$, $\hat4$ are the unit vector along $\rho-$direction, $4-$direction, respectively. $\eta_{x,\mu}$ is the staggered fermion phase.

We carry out simulations at $\theta = \mu_I/T = \pi$. As it is pointed out that the system is invariant under the charge conjugation at $\theta = 0, \pi$, when θ is fixed [9]. But the θ-odd quantity $O(\theta)$ is not invariant at $\theta = \pi$ under charge conjugation. When $T < T_{\mathrm{RW}}$, $O(\theta)$ is a smooth function of θ, so it is zero at $\theta = \pi$. Whereas when $T > T_{\mathrm{RW}}$, the two charge violating solutions cross each other at $\theta = \pi$. Thus the charge symmetry is spontaneously broken there and the θ-odd quantity $O(\theta)$ can be taken as order parameter. In this paper, we take the imaginary part of Polyakov loop as the order parameter.

The expression of Polyakov loop L is defined as the following:

$$\langle L\rangle = \left\langle \frac{1}{3L_s^3L_t}\sum_{\mathbf{x}}\mathrm{Tr}\left[\prod_{t=1}^{L_t}U_4(\mathbf{x},t)\right]\right\rangle.$$

L_s, L_t are the spatial, time extent of lattice, respectively. To simplify notation, we use X to represent the imaginary part of Polyakov loop $\mathrm{Im}(L)$. The susceptibility of imaginary part of Polyakov loop $\mathrm{Im}(L)$ is defined as

$$\chi = L_s^3\langle(X - \langle X\rangle)^2\rangle,$$

which is expected to scale as: [4,5]

$$\chi = L_s^{\gamma/\nu}\phi(\tau L_s^{1/\nu}), \tag{1}$$

where τ is the reduced temperature $\tau = (T - T_{\mathrm{RW}})/T_{\mathrm{RW}}$. This means that the curves $\chi/L_s^{\gamma/\nu}$ at different lattice volume should collapse with the same curve when plotted against $\tau L_s^{1/\nu}$. In the following, we employ $\beta - \beta_c$ in place of $\tau = (T - T_{\mathrm{RW}})/T_{\mathrm{RW}}$. The critical exponents relevant to our study are collected in Table I [5,30].

TABLE I. Critical exponents relevant to our study.

	$B_4(\beta_c,\infty)$	ν	γ	γ/ν
3D Ising	1.604	0.6301(4)	1.2372(5)	1.963
tricritical	2	1/2	1	2
first order	1.5	1/3	1	3
crossover	3	⋯	⋯	⋯

We also consider the Binder cumulant of imaginary part of Polyakov loop which is defined as the following:

$$B_4 = \langle (X - \langle X \rangle)^4 \rangle / \langle (X - \langle X \rangle)^2 \rangle^2 \tag{2}$$

with $\langle X \rangle = 0$. In the vicinity of the RW transition line endpoints, B_4 with the finite size correction is a function of $x = (\beta - \beta_{\rm RW}) L_s^{1/\nu}$ and can be expanded as a series [3,10,11],

$$B_4 = B_4(\beta_c, \infty) + a_1 x + a_2 x^2 + \cdots . \tag{3}$$

In the thermodynamic limit, the critical exponent ν and $B_4(\beta_c,\infty)$ takes on the corresponding value summarized in Table I. However, on finite spatial volumes, the steps of $B_4(\beta_c,\infty)$ are smeared out to continuous functions.

III. MC SIMULATION RESULTS

Before presenting the simulation results, we describe the simulation details. Simulations are carried out at quark mass $am = 0.024$, 0.026, 0.038, 0.040, 0.050, 0.060, 0.070. Rational Monte Carlo algorithm [31–33] is used to generate configurations. The Omelyan integration algorithm [34,35] is employed for the gauge and fermion action. For the molecular dynamics evolution we use a 9th rational function to approximate $[M^+(U)M(U)]^{-n_f/4}$ for the pseudofermion field. For the heat bath updating and for computing the action at the beginning and end of the molecular dynamics trajectory 10th rational function is used to approximate $[M^+(U)M(U)]^{n_f/8}$ and $[M^+(U)M(U)]^{-n_f/8}$, respectively. The step is chosen to ensure most of the acceptance rate is around 80%–90%. 5,000 trajectories of configuration are taken as warmup from a cold start. The simulation parameters are presented in Tables II and III. In order to fill in observables at additional β values, we employ the Ferrenberg-Swendsen reweighting method [36].

The critical coupling β_c's on various spatial volume at different quark mass am are summarized in Table IV. These β_c's are determined from the locations of peak susceptibility of imaginary part of Polyakov loop.

We present the rescaled susceptibility of imaginary part of Polyakov loop $\chi/L_s^{\gamma/\nu}$ as a function of $(\beta - \beta_c)L_s^{1/\nu}$ at $am = 0.024$ in Fig. 1. From Fig. 1, we can find that $\chi/L_s^{\gamma/\nu}$ according to the first order transition exponent collapses with the same curve, while $\chi/L_s^{\gamma/\nu}$ according to 3D Ising exponent does not.

The rescaled susceptibility of imaginary part of Polyakov loop $\chi/L_s^{\gamma/\nu}$ as a function of $(\beta - \beta_c)L_s^{1/\nu}$ at $am = 0.038$ is depicted in Fig. 2. From Fig. 2, we can find that $\chi/L_s^{\gamma/\nu}$ according to the first order transition exponent or 3D Ising exponent does not collapse with the same curve. We cannot determine the nature of Roberge-Weiss transition endpoint at $am = 0.038$ from $\chi/L_s^{\gamma/\nu}$.

The behavior of rescaled susceptibility of imaginary part of Polyakov loop $\chi/L_s^{\gamma/\nu}$ at $am = 0.040$ and $am = 0.070$ are presented in Fig. 3, and Fig. 4, respectively. Form Fig. 3 and Fig. 4, we can find that the rescaled susceptibility of imaginary part of Polyakov loop $\chi/L_s^{\gamma/\nu}$ at $am = 0.040$ and $am = 0.070$ have similar behavior to that at $am = 0.038$.

The rescaled susceptibility of imaginary part of Polyakov loop $\chi/L_s^{\gamma/\nu}$ as a function of $(\beta - \beta_c)L_s^{1/\nu}$ at $am = 0.050$ is depicted in Fig. 5. From Fig. 5, we can find that $\chi/L_s^{\gamma/\nu}$ as a function of $(\beta - \beta_c)L_s^{1/\nu}$ at lattice $12^3 \times 4$ and $16^3 \times 4$ are in favour of both first order transition exponent and 3D Ising exponent. However, considering the scale of $\chi/L_s^{\gamma/\nu}$ and $(\beta - \beta_c)L_s^{1/\nu}$ in Fig. 5, the first order transition exponent may be the better choice. $\chi/L_s^{\gamma/\nu}$ as a function of $(\beta - \beta_c)L_s^{1/\nu}$ at $am = 0.060$ has similar behavior to that at $am = 0.050$ which tends to be in favor of first order transition exponent.

In order to discern the scaling behavior, we turn to investigate Binder cumulant B_4 as defined in Eq. (2) whose scaling behavior is described in Eq. (3). B_4 decreases with the increase of β, and at one fixed quark mass am, B_4 as a function of β on various spatial volume is expected to intersect at one point. The intersection gives an estimate of accurate location of $\beta_{\rm RW}$. By fitting the values of B_4 to Eq. (3) with $B_4(\beta_c,\infty)$, a_1, a_2, $\beta_{\rm RW}$ and ν as parameters needed to be determined, we can extract critical exponent ν, $\beta_{\rm RW}$ and $B_4(\beta_c,\infty)$. The results are collected in Table V.

We present B_4 as a function of β at $am = 0.024$ in the left panel of Fig. 6, and B_4 as a function of $(\beta - \beta_{\rm RW})L_s^{1/\nu}$ in the right panel of Fig. 6 with ν taken to be the extracted value through fitting procedure. From Table V, we find that the critical exponent $\nu = 0.2410$ at $am = 0.024$ can explain the behavior of B_4 as a function of $(\beta - \beta_{\rm RW})L_s^{1/\nu}$, especially, on lattice $L_s = 16$, 20. This behavior implies that the transition endpoint at $am = 0.024$ belongs to first order transition.

We also present B_4 as a function of β at $am = 0.026$ in the left panel of Fig. 7, and B_4 as a function of $(\beta - \beta_{\rm RW})L_s^{1/\nu}$ in the right panel of Fig. 7 with ν taken to be the extracted value through fitting procedure. We find that the critical exponent $\nu = 0.6282$ at $am = 0.026$ can explain the behavior of B_4 as a function of $(\beta - \beta_{\rm RW})L_s^{1/\nu}$. $\nu = 0.6282$ suggests that the endpoint at $am = 0.026$ is of 3D Ising transition nature.

TABLE II. Simulation parameters. There are 10 molecular steps for every trajectory. 10 trajectories are taken between measurement. The autocorrelation time is calculated for $\mathrm{Im}(L)$. The columns marked with "β for B_4" and "β for χ" contain the β values for calculating B_4 and χ in terms of Ferrenberg-Swendsen reweighting method [36], respectively.

am	L_s	β	u_0	Step	# conf.	Accept.	Autocor. Time	$\mathrm{Im}(L)$	$\lvert L\rvert$	β for B_4	β for χ
0.024	12	6.480	0.892	0.042	800	0.88	89.1	0.031(27)	0.167(7)	6.480	6.480
	12	6.482	0.892	0.042	800	0.89	93.9	0.081(26)	0.176(10)	6.482	6.482
	12	6.484	0.892	0.042	800	0.88	311.1	0.048(34)	0.191(9)	6.484	6.484
	12	6.486	0.892	0.042	800	0.89	64.5	0.099(19)	0.167(9)	⋯	6.486
	12	6.488	0.892	0.042	800	0.89	105.1	−0.071(29)	0.185(9)	⋯	6.488
	12	6.500	0.892	0.047	800	0.85	11.2	0.161(10)	0.204(9)	⋯	6.500
	16	6.480	0.892	0.033	800	0.90	57.5	0.124(5)	0.166(5)	6.480	6.480
	16	6.482	0.892	0.033	800	0.90	60.9	0.123(11)	0.168(9)	6.482	6.482
	16	6.484	0.892	0.033	800	0.90	69.7	−0.140(7)	0.181(7)	6.484	6.484
	16	6.486	0.892	0.033	800	0.90	100.7	0.151(6)	0.192(6)	⋯	6.486
	16	6.488	0.892	0.033	800	0.90	80.1	0.141(11)	0.185(9)	⋯	6.488
	20	6.480	0.892	0.026	800	0.92	37.3	−0.106(16)	0.152(13)	6.480	⋯
	20	6.482	0.892	0.028	800	0.90	95.1	−0.104(10)	0.152(7)	6.482	6.482
	20	6.484	0.892	0.028	800	0.90	40.5	0.143(14)	0.184(13)	6.484	6.484
	20	6.488	0.892	0.028	800	0.89	32.8	0.153(6)	0.192(6)	⋯	6.488
0.026	12	6.486	0.892	0.042	2000	0.89	51.1	−0.109(21)	0.185(8)	6.486	⋯
	12	6.488	0.892	0.042	2000	0.88	289.8	−0.047(32)	0.189(8)	6.488	⋯
	12	6.490	0.892	0.042	2000	0.88	93.6	0.111(19)	0.180(7)	6.490	⋯
	16	6.478	0.892	0.033	2000	0.90	185.7	−0.034(20)	0.138(7)	6.478	⋯
	16	6.480	0.892	0.033	2000	0.90	206.1	−0.055(21)	0.146(8)	6.480	⋯
	16	6.486	0.892	0.033	2000	0.91	211.1	0.093(16)	0.156(8)	6.486	⋯
	20	6.482	0.892	0.028	2000	0.90	150.4	0.020(23)	0.143(7)	6.482	⋯
	20	6.484	0.892	0.028	2000	0.90	103.9	−0.122(8)	0.165(6)	6.484	⋯
	20	6.486	0.892	0.028	2000	0.90	212.3	0.008(20)	0.129(7)	6.486	⋯
	20	6.488	0.892	0.028	2000	0.91	157.7	0.090(8)	0.140(6)	6.488	⋯
0.038	12	6.820	0.856	0.042	1000	0.89	20.3	−0.084(13)	0.146(9)	⋯	6.820
	12	6.825	0.856	0.042	1000	0.89	33.9	−0.103(26)	0.169(15)	⋯	6.825
	12	6.835	0.856	0.042	1000	0.88	33.6	0.160(23)	0.215(13)	⋯	6.835
	12	6.840	0.856	0.042	1000	0.88	47.5	0.090(42)	0.196(13)	⋯	6.840
	12	6.860	0.892	0.059	1000	0.75	3.0	0.385(2)	0.447(2)	⋯	6.860
	16	6.805	0.856	0.034	1000	0.89	23.8	−0.115(8)	0.157(7)	6.805	6.805
	16	6.810	0.856	0.034	1000	0.89	141.4	−0.123(14)	0.167(12)	6.810	6.810
	16	6.815	0.856	0.034	1000	0.89	55.0	−0.079(20)	0.140(13)	6.815	6.815
	16	6.820	0.856	0.034	1000	0.89	147.5	0.127(16)	0.172(13)	6.820	6.820
	16	6.825	0.856	0.034	1000	0.89	71.2	−0.152(9)	0.193(9)	6.825	6.825
	16	6.830	0.856	0.034	1000	0.89	7.9	0.193(4)	0.233(4)	6.830	6.830
	20	6.805	0.856	0.028	1000	0.91	47.6	0.131(8)	0.170(7)	6.805	6.805
	20	6.815	0.856	0.028	1000	0.90	31.0	0.088(11)	0.137(8)	6.815	6.815
	20	6.820	0.856	0.028	1000	0.90	45.3	−0.071(16)	0.132(9)	6.820	6.820
	20	6.830	0.856	0.028	1000	0.90	94.1	−0.143(16)	0.188(12)	6.830	6.830
	20	6.835	0.856	0.028	1000	0.91	47.2	−0.158(7)	0.198(7)	6.835	6.835
	20	6.840	0.856	0.028	1000	0.91	81.7	−0.165(5)	0.205(5)	6.840	6.840
0.040	12	6.825	0.856	0.042	1000	0.89	107.2	0.093(44)	0.200(12)	6.825	6.825
	12	6.830	0.856	0.042	1000	0.89	103.4	0.068(39)	0.177(13)	6.830	⋯
	12	6.835	0.856	0.042	1000	0.88	55.0	−0.069(47)	0.195(17)	6.835	6.835
	12	6.840	0.856	0.042	1000	0.89	12.7	0.175(7)	0.216(6)	⋯	6.840
	12	6.845	0.856	0.042	1000	0.89	128.5	−0.093(49)	0.215(11)	6.845	6.845
	12	6.850	0.892	0.059	1000	0.75	2.4	−0.388(2)	0.450(2)	⋯	6.850
	16	6.810	0.856	0.034	1000	0.89	42.1	0.135(8)	0.175(8)	⋯	6.810
	16	6.830	0.856	0.034	1000	0.89	107.3	0.162(11)	0.202(11)	⋯	6.830
	16	6.840	0.856	0.034	1000	0.90	57.4	−0.122(19)	0.171(17)	⋯	6.840
	16	6.850	0.892	0.059	1000	0.61	2.6	0.386(1)	0.448(1)	⋯	6.850

TABLE III. Simulation parameters. There are 10 molecular steps for every trajectory. 10 trajectories are taken between measurement. The autocorrelation time is calculated for $\mathrm{Im}(L)$. The columns marked with "β for B_4" and "β for χ" contain the β values for calculating B_4 and χ in terms of Ferrenberg-Swendsen reweighting method [36], respectively.

am	L_s	β	u_0	Step	# conf.	Accept.	Autocor. Time	$\mathrm{Im}(L)$	$\lvert L\rvert$	β for B_4	β for χ
0.040	20	6.810	0.856	0.028	1000	0.90	47.0	0.019(6)	0.098(2)	6.810	···
	20	6.815	0.856	0.028	1000	0.91	35.5	−0.032(9)	0.105(3)	6.815	···
	20	6.820	0.856	0.028	1000	0.90	37.9	−0.101(7)	0.146(6)	6.820	···
	20	6.830	0.856	0.028	1000	0.91	64.4	0.144(9)	0.186(8)	···	6.830
	20	6.840	0.856	0.028	1000	0.90	80.7	−0.009(18)	0.117(6)	···	6.840
	20	6.845	0.856	0.028	1000	0.91	18.3	−0.186(6)	0.226(5)	···	6.845
	20	6.850	0.892	0.059	1000	0.50	6.6	0.383(2)	0.445(2)	···	6.850
0.050	12	6.800	0.858	0.042	1000	0.88	27.9	−0.011(29)	0.137(6)	6.800	6.800
	12	6.820	0.858	0.042	1000	0.89	45.3	−0.064(23)	0.149(8)	6.820	6.820
	12	6.840	0.858	0.042	1000	0.89	81.0	−0.004(52)	0.199(13)	6.840	6.840
	12	6.860	0.858	0.042	1000	0.89	38.1	0.127(25)	0.189(17)	6.860	6.860
	12	6.880	0.858	0.042	1000	0.89	22.4	0.192(15)	0.237(14)	6.880	6.880
	16	6.810	0.858	0.034	1000	0.89	21.3	−0.104(10)	0.149(9)	6.810	6.810
	16	6.830	0.858	0.034	1000	0.90	149.9	0.023(39)	0.164(8)	6.830	6.830
	16	6.840	0.858	0.034	1000	0.90	39.2	0.147(12)	0.191(12)	···	6.840
	16	6.850	0.858	0.034	1000	0.89	137.3	0.076(38)	0.175(15)	6.850	6.850
	20	6.830	0.858	0.028	1000	0.91	63.8	0.038(25)	0.132(10)	6.830	···
	20	6.840	0.858	0.028	1000	0.91	112.2	−0.121(11)	0.167(9)	6.840	6.840
	20	6.850	0.858	0.028	1000	0.91	40.2	0.167(10)	0.209(9)	6.850	6.850
	20	6.860	0.858	0.028	1000	0.91	79.1	−0.163(10)	0.206(10)	6.860	6.860
	20	6.870	0.858	0.028	1000	0.91	27.3	−0.189(4)	0.230(4)	6.870	6.870
0.060	12	6.840	0.860	0.042	1000	0.89	17.4	0.138(11)	0.187(9)	6.840	6.840
	12	6.850	0.860	0.042	1000	0.89	49.1	−0.109(21)	0.167(15)	6.850	6.850
	12	6.860	0.860	0.042	1000	0.89	51.8	−0.130(20)	0.179(18)	6.860	6.860
	12	6.870	0.860	0.042	1000	0.89	59.8	−0.059(48)	0.203(15)	6.870	6.870
	12	6.880	0.860	0.042	1000	0.89	13.0	−0.212(10)	0.255(10)	6.880	6.880
	16	6.850	0.860	0.034	1000	0.90	144.0	−0.004(32)	0.145(11)	···	6.850
	16	6.860	0.860	0.034	1000	0.89	61.6	0.186(9)	0.229(8)	···	6.860
	16	6.870	0.860	0.034	1000	0.90	30.3	−0.184(8)	0.227(8)	···	6.870
	16	6.880	0.860	0.034	1000	0.90	77.2	−0.204(9)	0.245(10)	···	6.880
	20	6.820	0.860	0.028	1000	0.91	50.9	−0.048(14)	0.116(8)	6.820	6.820
	20	6.830	0.860	0.028	1000	0.91	44.0	0.020(10)	0.102(3)	6.830	6.830
	20	6.850	0.860	0.028	1000	0.91	30.6	0.130(6)	0.172(6)	6.850	6.850
	20	6.870	0.860	0.028	1000	0.91	26.9	−0.178(7)	0.221(7)	6.870	6.870
	20	6.890	0.860	0.028	1000	0.91	53.2	0.225(7)	0.269(7)	6.890	6.890
0.070	12	6.820	0.861	0.042	1000	0.89	26.9	−0.049(17)	0.125(8)	6.820	···
	12	6.830	0.861	0.042	1000	0.89	75.6	0.009(26)	0.135(9)	6.830	6.830
	12	6.850	0.861	0.042	1000	0.88	53.5	−0.033(38)	0.161(14)	6.850	6.850
	12	6.860	0.861	0.042	1000	0.89	57.8	−0.016(26)	0.137(8)	6.860	6.860
	12	6.870	0.861	0.042	1000	0.89	54.7	0.090(36)	0.188(12)	···	6.870
	12	6.880	0.861	0.042	1000	0.89	20.2	−0.168(15)	0.215(14)	···	6.880
	16	6.860	0.861	0.034	1000	0.90	46.7	−0.092(17)	0.149(13)	···	6.860
	16	6.870	0.861	0.034	1000	0.90	19.3	0.171(10)	0.214(9)	···	6.870
	16	6.880	0.861	0.034	1000	0.90	146.3	−0.129(23)	0.186(16)	···	6.880
	16	6.900	0.861	0.034	1000	0.89	18.5	−0.202(6)	0.246(6)	···	6.900
	20	6.810	0.861	0.029	1000	0.89	50.4	0.017(11)	0.098(3)	6.810	···
	20	6.820	0.861	0.029	1000	0.89	107.3	0.018(9)	0.098(2)	6.820	6.820
	20	6.830	0.861	0.029	1000	0.89	66.9	−0.006(6)	0.096(1)	6.830	6.830
	20	6.840	0.861	0.029	1000	0.89	53.0	0.040(17)	0.118(8)	6.840	6.840
	20	6.850	0.861	0.029	1000	0.89	50.8	0.070(7)	0.126(5)	6.850	6.850
	20	6.860	0.861	0.029	1000	0.89	54.6	−0.105(10)	0.153(9)	···	6.860
	20	6.870	0.861	0.029	1000	0.89	45.7	−0.016(12)	0.112(3)	···	6.870

TABLE IV. Results of critical couplings β_c on different spatial volume at different quark mass.

am	12	16	20
0.024	6.492(9)	6.491(8)	6.4834(15)
0.038	6.838(4)	6.821(4)	6.824(3)
0.040	6.839(3)	6.839(3)	6.847(2)
0.050	6.845(10)	6.831(7)	6.857(4)
0.060	6.859(9)	6.865(5)	6.860(3)
0.070	6.875(7)	6.885(6)	6.857(4)

At $am = 0.040$, we only find that B_4 as a function of β on lattice $L_s = 12$, 20 intersects at one point. B_4 as a function of β and as a function of $(\beta - \beta_{\mathrm{RW}})L_s^{1/\nu}$ at $am = 0.040$ are depicted in the left, right panel of Fig. 8, respectively. The extracted value $\nu = 0.6173$ through fitting procedure also shows that the endpoint at $am = 0.040$ is of 3D Ising transition nature. At other values of am, B_4 as a function of β and as a function of $(\beta - \beta_{\mathrm{RW}})L_s^{1/\nu}$ have similar behavior. For clarity, they are not presented.

From the behavior of $\chi/L_s{}^{\gamma/\nu}$ and B_4, we conclude that the nature of endpoint transition at $am = 0.024$, 0.050, 0.060, 0.070 is of first order, while at $am = 0.026, 0.038, 0.040$, the endpoint transition nature is of 3D Ising class. This conclusion suggests that the two tricritical points are between $0.024 < am_{\mathrm{tricl}} < 0.026$ and $0.040 < am_{\mathrm{tricl}} < 0.050$.

IV. DISCUSSIONS

We have studied the nature of critical endpoints of Roberge-Weiss transition of two flavor lattice QCD with improved Kogut-Susskind fermions. When $i\mu_I = i\pi T$, the imaginary part of the Polayakov loop is the order parameter for studying the transition from low temperature phase to high temperature one.

Our simulations are carried out at 7 values of quark mass am on $L_t = 4$ lattice on different 3 spatial volumes. Our

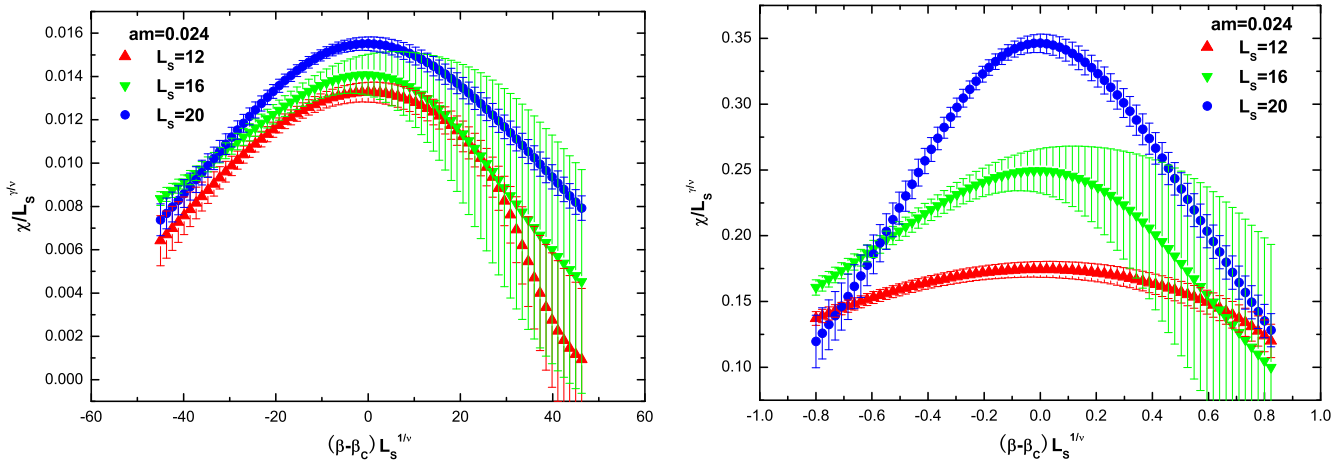

FIG. 1. Scaling behavior of the susceptibility of imaginary part of Polyakov loop according to first order critical exponent (left panel), and to 3D Ising critical exponent (right panel) at $am = 0.024$.

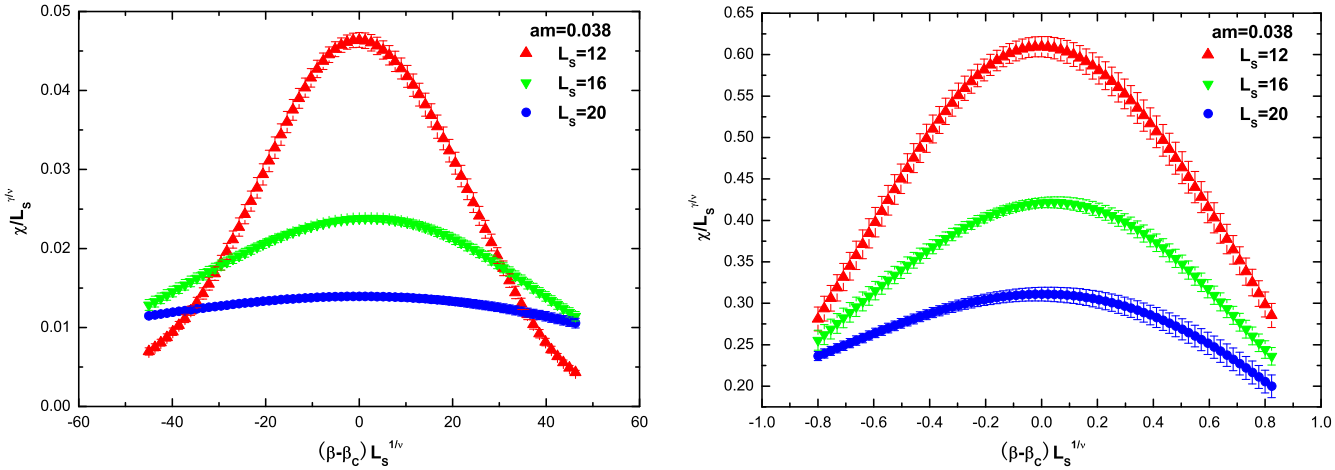

FIG. 2. Scaling behavior of the susceptibility of imaginary part of Polyakov loop according to first order critical exponent (left panel), and to 3D Ising critical exponent (right panel) at $am = 0.038$.

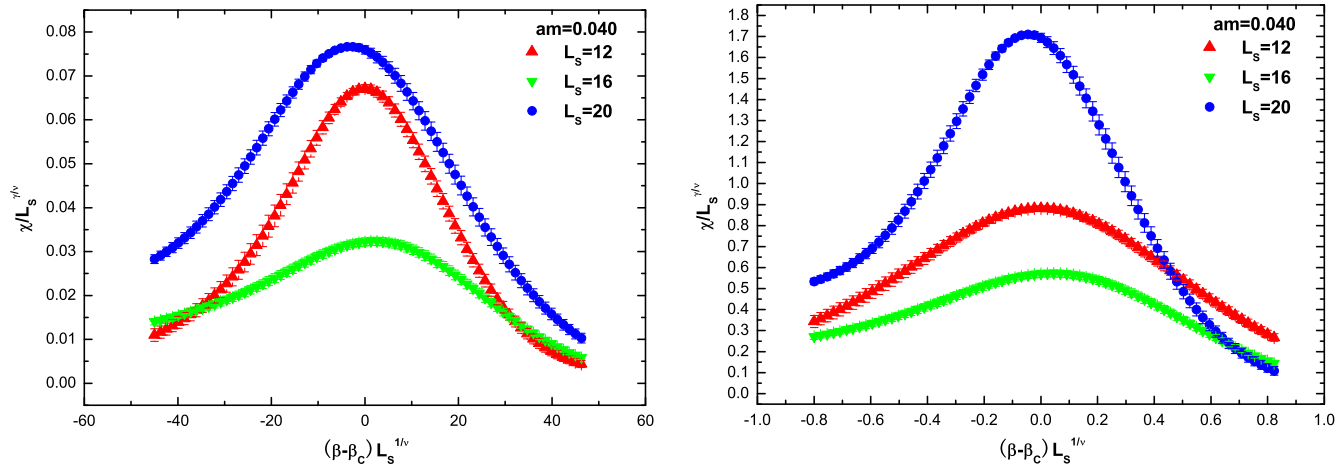

FIG. 3. Scaling behavior of the susceptibility of imaginary part of Polyakov loop according to first order critical exponent (left panel), and to 3D Ising critical exponent (right panel) at $am = 0.040$.

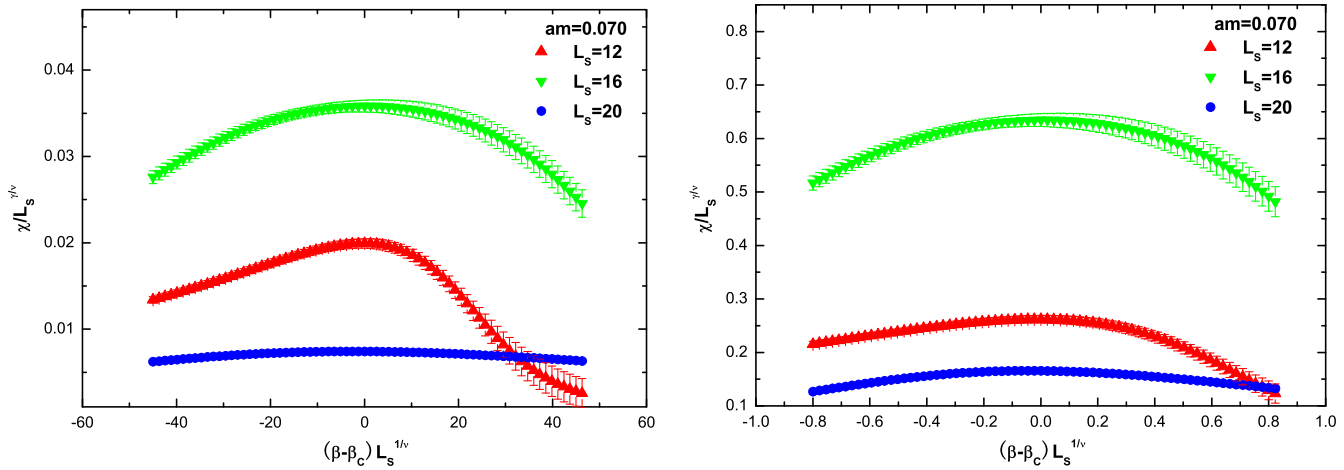

FIG. 4. Scaling behavior of the susceptibility of imaginary part of Polyakov loop according to first order critical exponent (left panel), and to 3D Ising critical exponent (right panel) at $am = 0.070$.

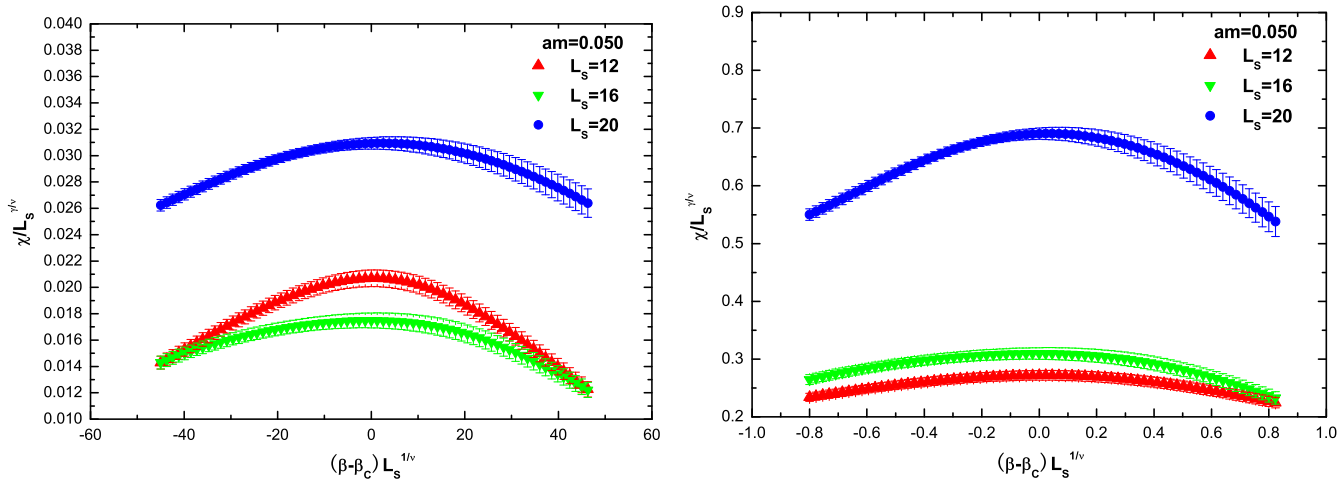

FIG. 5. Scaling behavior of the susceptibility of imaginary part of Polyakov loop according to first order critical exponent (left panel), and to 3D Ising critical exponent (right panel) at $am = 0.050$.

TABLE V. Results of critical couplings β_{RW} and the critical exponent ν by fitting Eq. (3) to data on different spatial volume. If errors are very small, we take them to be zero.

am	L_s	β_{RW}	ν	$B_4(\beta_c,\infty)$	a_1	a_2	r-square
0.024	12, 16, 20	6.4816(0)	0.2410(8)	2.2661(11)	−0.0022(0)	0.000(0)	0.991
0.026	12, 16, 20	6.4825(0)	0.6282(3)	1.71958(6)	−0.7061(14)	0.2033(9)	0.996
0.038	16, 20	6.8503(0)	0.6473(17)	1.0300(0)	−0.0363(4)	0.01145(2)	0.996
0.040	12, 20	6.8185(0)	0.6173(4)	2.1039(3)	−1.053(3)	0.136(8)	0.998
0.050	12, 16, 20	6.831(0)	0.3691(6)	1.8924(2)	−0.0295(4)	0.0008(0)	0.992
0.060	12, 20	6.8416(0)	0.3458(19)	1.6937(10)	−0.0125(6)	–	0.958
0.070	12, 20	6.8416(0)	0.3152(6)	2.1821(2)	−0.005(0)	–	0.936

central result is that the two tricritical points are between $0.024 < am_{\mathrm{tricl}} < 0.026$ and $0.040 < am_{\mathrm{tricl}} < 0.050$. The interval of quark mass from 0.024 to 0.026 is narrow. On finite spatial volume, the exponent ν is expected to change smoothly, while our simulation shows that exponent ν changes rapidly within a narrow quark mass interval.

Apart from monitoring the behavior of susceptibility of imaginary part of Polayakov loop $\mathrm{Im}(L)$, we also look into the change of Binder cumulant of $\mathrm{Im}(L)$. In order to fill in observables at additional β values, the Ferrenberg-Swendsen reweighting method [36] is employed. It is noted that when applying Ferrenberg-Swendsen reweighting

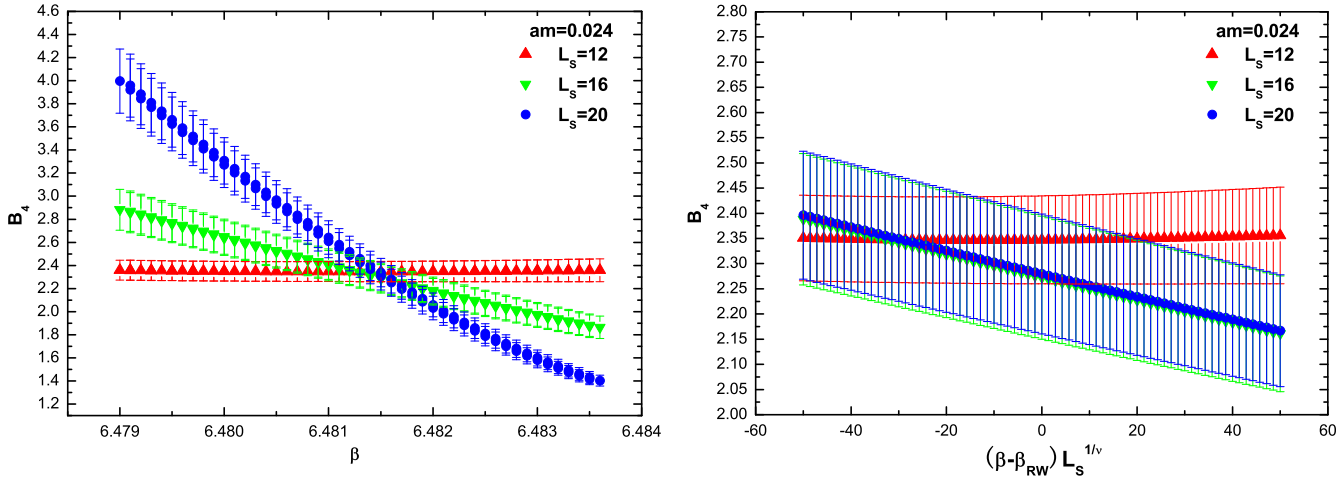

FIG. 6. Binder cumulants as a function of β on various spatial volume intersect at one point (left panel), and as a function of $(\beta-\beta_{\mathrm{RW}})L_s^{1/\nu}$ with values of β_{RW}, ν from Table V collapse (right panel) at $am = 0.024$.

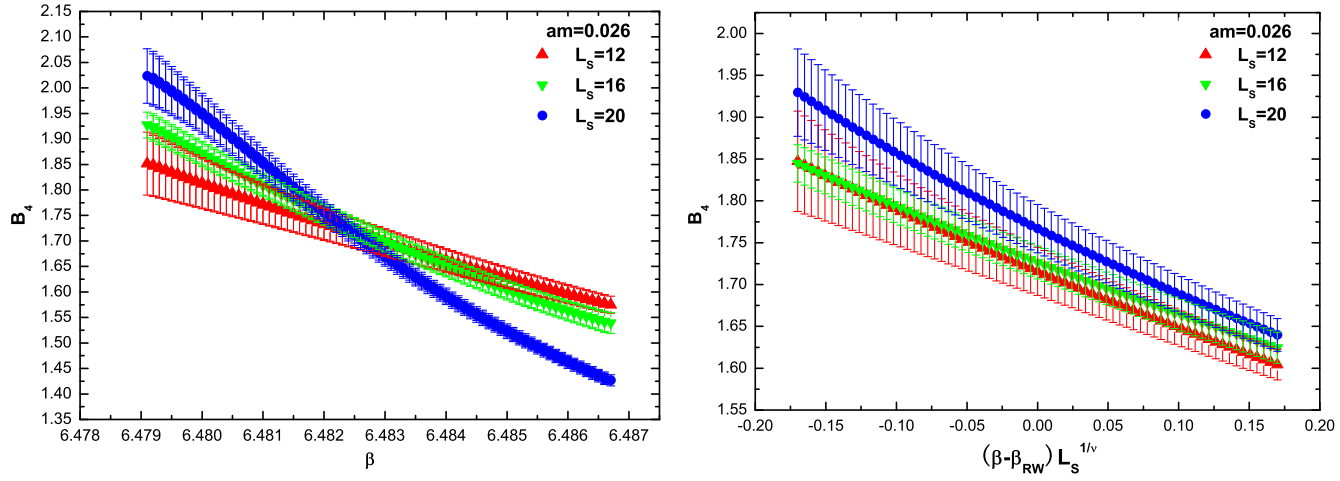

FIG. 7. Binder cumulants as a function of β on various spatial volume intersect at one point (left panel), and as a function of $(\beta-\beta_{\mathrm{RW}})L_s^{1/\nu}$ with values of β_{RW}, ν from Table V collapse (right panel) at $am = 0.026$.

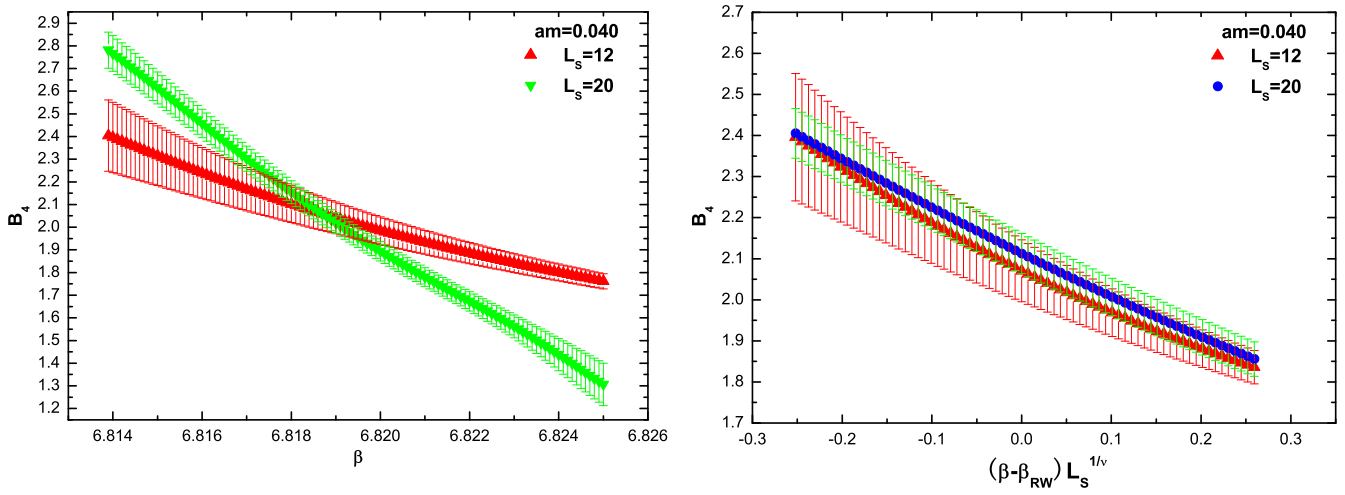

FIG. 8. Binder cumulants as a function of β on various spatial volume intersect at one point (left panel), and as a function of $(\beta-\beta_{\mathrm{RW}})L_s^{1/\nu}$ with values of β_{RW}, ν from Table V collapse (right panel) at $am=0.040$.

method, the number of β points taken to calculate susceptibility is not completely the same as the number taken to calculate Binder cumulant.

In our simulations, the behavior of susceptibility of imaginary part of Polayakov loop $\mathrm{Im}(L)$ at $am=0.024$ can give us clear signal to determine the nature of transition, while at other quark masses, it is difficult to determine the nature of transition.

The values of $B_4(\beta_c,\infty)$ extracted through fitting procedure are inconsistent with what is expected. This is because logarithmic scaling corrections will be present near the tricritical point [3,37], and our simulations are carried out on finite size volume on which large finite size corrections are observed in simpler spin model [38]. However, the critical exponent ν is not sensitive to finite size corrections [3]. So exponent ν extracted through fitting procedure can provide us information to determine the transition nature.

In our simulation, we can find that the values of B_4 on lattice with spatial volumes 12^3, 16^3, 20^3 intersect approximately at one point at quark masses $am=0.024$, 0.026, 0.050, while at other quark masses, it is difficult to find intersection point for B_4's from three spatial volumes. It is expedient to determine the intersection point from two spatial volumes as indicated in Table V.

Taking what is mentioned above into account, further work along this direction which can provide crosschecks is expected, especially simulations with larger time extent which is under our consideration.

ACKNOWLEDGMENTS

We thank Philippe de Forcrand for valuable helps. We modify the MILC collaboration's public code [39] to simulate the theory at imaginary chemical potential. We use the fortran-90 based multi-precision software [40]. This work is supported by the National Natural Science Foundation of China (NSFC) under Grant No. 11347029. The work was carried out at National Supercomputer Center in Wuxi; we appreciate the help of Qiong Wang and Zhao liu when carrying out the computation.

[1] K. Fukushima and T. Hatsuda, The phase diagram of dense QCD, Rept. Prog. Phys. **74**, 014001 (2011).
[2] K. Fukushima, QCD matter in extreme environments, J. Phys. G **39**, 013101 (2012).
[3] P. de Forcrand and O. Philipsen, Constraining the QCD Phase Diagram by Tricritical Lines at Imaginary Chemical Potential, Phys. Rev. Lett. **105**, 152001 (2010).
[4] M. D'Elia and F. Sanfilippo, The order of the Roberge-Weiss endpoint (finite size transition) in QCD, Phys. Rev. D **80**, 111501 (2009).
[5] C. Bonati, G. Cossu, M. D'Elia, and F. Sanfilippo, The Roberge-Weiss endpoint in $N_f=2$ QCD, Phys. Rev. D **83**, 054505 (2011).
[6] M. D'Elia, F. Di Renzo, and M. P. Lombardo, The strongly interacting quark gluon plasma, and the critical behaviour of QCD at imaginary μ, Phys. Rev. D **76**, 114509 (2007).
[7] Y. Sakai, H. Kouno, and M. Yahiro, QCD phase diagram at imaginary baryon and isospin chemical potentials, J. Phys. G **37**, 105007 (2010).

[8] G. Aarts, S. P. Kumar, and J. Rafferty, Holographic Roberge-Weiss transitions, J. High Energy Phys. 07 (2010) 056.
[9] H. Kouno, Y. Sakai, K. Kashiwa, and M. Yahiro, The Roberge-Weiss phase transition and its endpoint, J. Phys. G **36**, 115010 (2009).
[10] O. Philipsen and P. de Forcrand, Constraints for the QCD phase diagram from imaginary chemical potential, *Proc. Sci.* LATTICE2010 (2010) 211, [arXiv:1011.0291].
[11] C. Bonati, P. de Forcrand, M. D'Elia, O. Philipsen, and F. Sanfilippo, Constraints on the two-flavor QCD phase diagram from imaginary chemical potential, *Proc. Sci.* LATTICE 2011 (2011) 189, [arXiv:1201.2769].
[12] A. Roberge and N. Weiss, Gauge theories with imaginary chemical potential and the phases of QCD, Nucl. Phys. **B275**, 734 (1986).
[13] P. de Forcrand and O. Philipsen, The QCD phase diagram for small densities from imaginary chemical potential, Nucl. Phys. **B642**, 290 (2002).
[14] M. D'Elia and M.-P. Lombardo, Finite density QCD via imaginary chemical potential, Phys. Rev. D **67**, 014505 (2003).
[15] O. Philipsen and C. Pinke, Nature of the Roberge-Weiss transition in $N_f = 2$ QCD with Wilson fermions, Phys. Rev. D **89**, 094504 (2014).
[16] L. K. Wu and X. F. Meng, Nature of Roberge-Weiss transition endpoints for heavy quarks in $N_f = 2$ lattice QCD with Wilson fermions, Phys. Rev. D **90**, 094506 (2014).
[17] P. de Forcrand and O. Philipsen, The chiral critical line of $N(f) = 2 + 1$ QCD at zero and non-zero baryon density, J. High Energy Phys. 01 (2007) 077.
[18] P. de Forcrand and O. Philipsen, The chiral critical point of $N(f) = 3$ QCD at finite density to the order $(\mu/T)^4$, J. High Energy Phys. 11 (2008) 012.
[19] C. Bonati, P. de Forcrand, M. D'Elia, O. Philipsen, and F. Sanfilippo, Chiral phase transition in two-flavor QCD from an imaginary chemical potential, Phys. Rev. D **90**, 074030 (2014).
[20] K. Symanzik, Continuum limit and improved action in lattice theories. 1. Principles and φ^4 theory, Nucl. Phys. **B226**, 187 (1983).
[21] M. Luscher and P. Weisz, Computation of the action for on-shell improved lattice gauge theories at weak coupling, Phys. Lett. B **158B**, 250 (1985).
[22] G. P. Lepage and P. B. Mackenzie, Viability of lattice perturbation theory, Phys. Rev. D **48**, 2250 (1993).
[23] M. G. Alford, W. Dimm, G. P. Lepage, G. Hockney, and P. B. Mackenzie, Lattice QCD on small computers, Phys. Lett. B **361**, 87 (1995).
[24] T. Blum, C. DeTar, S. Gottlieb, K. Rummukainen, U. M. Heller, J. E. Hetrick, D. Toussaint, R. L. Sugar, and M. Wingate, Improving flavor symmetry in the Kogut-Susskind hadron spectrum, Phys. Rev. D **55**, R1133 (1997).
[25] K. Orginos, D. Toussaint, and R. L. Sugar (MILC Collaboration), Variants of fattening and flavor symmetry restoration, Phys. Rev. D **60**, 054503 (1999).
[26] A. Bazavov *et al.*, The chiral and deconfinement aspects of the QCD transition, Phys. Rev. D **85**, 054503 (2012).
[27] A. Bazavov *et al.* (MILC Collaboration), Nonperturbative QCD simulations with $2 + 1$ flavors of improved staggered quarks, Rev. Mod. Phys. **82**, 1349 (2010).
[28] S. Naik, On-shell improved lattice action for QCD with Susskind fermions and asymptotic freedom scale, Nucl. Phys. **B316**, 238 (1989).
[29] C. W. Bernard *et al.* (MILC Collaboration), Quenched hadron spectroscopy with improved staggered quark action, Phys. Rev. D **58**, 014503 (1998).
[30] A. Pelissetto and E. Vicari, Critical phenomena and renormalization group theory, Phys. Rep. **368**, 549 (2002).
[31] M. A. Clark and A. D. Kennedy, The RHMC algorithm for two flavors of dynamical staggered fermions, Nucl. Phys. B, Proc. Suppl. **129**, 850 (2004).
[32] M. A. Clark and A. D. Kennedy, Accelerating staggered fermion dynamics with the rational hybrid Monte Carlo algorithm, Phys. Rev. D **75**, 011502 (2007).
[33] M. A. Clark and A. D. Kennedy, Accelerating Dynamical Fermion Computations Using the Rational Hybrid Monte Carlo Algorithm with Multiple Pseudofermion Fields, Phys. Rev. Lett. **98**, 051601 (2007).
[34] T. Takaishi and P. de Forcrand, Testing and tuning symplectic integrators for hybrid Monte Carlo algorithm in lattice QCD, Phys. Rev. E **73**, 036706 (2006).
[35] I. P. Omeylan, I. M. Mryglod, and R. Folk, Symplectic analytically integrable decomposition algorithms: classification, derivation, and application to molecular dynamics, quantum and celestial mechanics simulations, Comput. Phys. Commun. **151**, 272 (2003).
[36] A. M. Ferrenberg and R. H. Swendsen, Optimized Monte Carlo Analysis, Phys. Rev. Lett. **63**, 1195 (1989).
[37] I. D. Lawrie and S. Sarbach, in *Phase Transitions and Critical Phenomena*, edited by C. Domb and J. L. Lebowitz (Academic Press, New York, 1984), Vol. 9, p. 1.
[38] A. Billoire, T. Neuhaus, and B. Berg, Observation of FSS for a first order phase transition, Nucl. Phys. **B396**, 779 (1993).
[39] http://physics.utah.edu/~detar/milc/.
[40] http://crd-legacy.lbl.gov/~dhbailey/mpdist/.